frontiers | Frontiers in Materials

ORIGINAL RESEARCH
published: 28 June 2022
doi: 10.3389/fmats.2022.914009

Evaluation of Cytotoxicity of Pb^{2+} Ion-Adsorbed Amino-Functionalized Magnetic Mesoporous Silica Nanoparticles: An *In Vitro* Study

*Yu Chen and Miao Liu**

College of New Energy and Environment, Jilin University, Changchun, China

Application of amino-functionalized mesoporous silica-coated core-shell magnetic nanoparticles (Fe_3O_4@mSiO_2-NH_2 NPs) for adsorbing heavy metal ions has attracted intensive interest in recent years. Despite the cytotoxicity triggered by the co-exposure of nanoparticles (NPs) and metal ions in relatively high dosages being reported, the effect of the adsorbed heavy metal ions on the cytotoxicity to human cells remains unexplored. Herein, we demonstrated the effect of amino-functionalized Fe_3O_4@mSiO_2 core-shell magnetic nanoparticles before and after adsorbing Pb^{2+} ions on the cytotoxicity of human kidney cells (HEK293). The surface morphology, viability, and oxidative stress (OS) induction of HEK293 cells incubated with Fe_3O_4@mSiO_2-NH_2 NPs and Pb^{2+} ion-adsorbed Fe_3O_4@mSiO_2-NH_2 NPs were assessed, respectively. Transmission electron microscopic (TEM) images of cell sections depicted that Fe_3O_4@mSiO_2-NH_2 NPs were internalized by HEK293 cells and gathered mainly in the cytoplasm. Cell viability (MTT) assays revealed the Fe_3O_4@mSiO_2-NH_2 NPs could enhance the cell viability to 119.9% and 108.2% compared to the control group, respectively. On contrast, the Pb^{2+} ion-adsorbed Fe_3O_4@mSiO_2-NH_2 NPs were toxic to the cell because when the Pb^{2+} ion contents were 5.0 and 7.5 μg mL^{-1}, the viabilities of the samples decreased to 97.1% and 84.7%, respectively. Oxidative stress data proved that OS was negatively affected by both dissociative Pb^{2+} ions and the Pb^{2+} ion-adsorbed Fe_3O_4@mSiO_2-NH_2 NPs. Cytotoxicity may be attributed to the OS induced by Pb^{2+} ions leaked from the adsorbent. Under the same Pb^{2+} ion concentration, the cytotoxicity of the adsorbed Pb^{2+} ions was lower than that of the dissociative Pb^{2+} ions, indicating that the adsorption by NPs inhibited the cytotoxicity of Pb^{2+} ions. This work will provide new references for assessing the cytotoxicity of Pb^{2+}-adsorbed nanoparticles.

Keywords: magnetic, nanoparticles, lead ions, adsorption, cytotoxicity, HEK293 cells

OPEN ACCESS

Edited by:
Anuj Kumar,
Yeungnam University, South Korea

Reviewed by:
Yougen Yi,
Central South University, China
Tao Xian,
Qinghai Normal University, China

****Correspondence:***
Miao Liu
liumiao@jlu.edu.cn

Specialty section:
This article was submitted to Biomaterials, a section of the journal Frontiers in Materials

Received: *06 April 2022*
Accepted: *19 May 2022*
Published: *28 June 2022*

Citation:
Chen Y and Liu M (2022) Evaluation of Cytotoxicity of Pb^{2+} Ion-Adsorbed Amino-Functionalized Magnetic Mesoporous Silica Nanoparticles: An In Vitro Study. Front. Mater. 9:914009. doi: 10.3389/fmats.2022.914009

INTRODUCTION

With the improvement of human life quality, the dependence of humans on lead-containing batteries and electronic products is becoming more and more serious, leading to the serious pollution of lead ions in the environment (Pandey et al., 2020). When these products are eliminated, they will be buried as solid waste, which will flow into rivers and lakes with rainfall and pollute water resources (Sharma et al., 2020). With the discharge of industrial wastewater, the permanent toxicity of lead has

been a major concern for human beings (Brännvall et al., 1999). Pb^{2+} ions cannot be biodegraded in human organisms and will cause numerous diseases and disorders (Inglezakis et al., 2003; Li et al., 2005; Maria das Graças et al., 2006). In addition, Pb^{2+} ions are enzyme inhibitors and accumulate in the bones, brain, kidneys, and muscles (Li et al., 2005). Patrick (2006) pointed out that the Pb^{2+} ions of concentrations higher than 10 μg dL^{-1} were considered to be deleterious. Therefore, it is of great significance to develop a new semiconductor material to remove Pb^{2+} ions.

Recently, a variety of engineered magnetic nanoparticles (MNPs) have been applied in magnetic separation photocatalysts, magnetic recording media, medical research, and wastewater treatments (Slowing et al., 2008; Facchi et al., 2018; Wang S. F et al., 2021). To avoid the accumulation of magnetic nanoparticles, core-shell and other composite nanostructures have been developed by a special preparation method. (Liu et al., 2020; Tang et al., 2020; Cheng et al., 2022a; Li et al., 2022a; Li et al., 2022b). The mesoporous silica coatings around the MNPs are applied in the synthesis process, which also provide a convenient base to graft-specific ligands. Therefore, the magnetic mesoporous nanoparticles are extensively exploited in heavy metal ions or dye adsorption because of their high specific surface area, ease of modification, and collection (Zhang C et al., 2014; Almasian et al., 2016; Gao et al., 2021). To enhance the adsorption ability of heavy metal ions (usually are cations), amino groups are modified onto the mesoporous silica coating surface *via* a silanization process (Ma et al., 2019). However, it gradually draws our attention that the heavy metal ion–adsorbed MNPs are still risky to human health because of their extremely small particle size which is capable of entering into human cells (Bundschuh et al., 2018). Researchers suggest that MNPs can affect the morphology of cells, leading to apoptosis and the damage of DNA through oxidative stress (OS) (He and Park, 2016). This process will be affected by a series of factors, such as concentration, particle size, surface functional group, and the degree of dispersion of nanoparticles (NPs) (Wang et al., 2018; Di et al., 2021; Krętowski et al., 2021; Sun et al., 2021; Cheng et al., 2022b; Liu et al., 2022; Xian et al., 2022). For example, the grafted amino groups could prevent superparamagnetic iron oxide (SPIO) nanoparticles from aggregating in DMEM and promote the cellular uptake efficiency without increasing the cytotoxicity (Zhu et al., 2012).

Despite researchers noticing the unique toxicity of the co-exposure of nanoparticles and Pb^{2+} ions (Lu et al., 2015; Feng et al., 2018; Ahamed et al., 2019), the cytotoxicity of Pb^{2+} ion-adsorbed amino-functionalized magnetic mesoporous silica (Fe_3O_4@$mSiO_2$-NH_2) NPs with size above 100 nm has not yet been reported. In this study, we synthesized Fe_3O_4@$mSiO_2$-NH_2 NPs with good ability for adsorption of Pb^{2+} ions (**Scheme 1**). Then, the Fe_3O_4@$mSiO_2$-NH_2 NPs with and without the adsorption of Pb^{2+} ions were chosen to prepare the culture media, which were used for the incubation of HEK293 cells. To evaluate the cytotoxicity of Pb^{2+} ion-adsorbed NPs, the cell viability (MTT) and morphology were investigated. Reactive oxygen species (ROS) and malondialdehyde (MDA) levels, superoxide dismutase enzyme (SOD), and glutathione peroxidase (GSH-Px) activity were measured to explore the inner mechanism of the Pb^{2+} ion-adsorbed Fe_3O_4@$mSiO_2$-NH_2 NP-induced cytotoxicity.

EXPERIMENT

Materials

Ferric chloride hexahydrate ($FeCl_3.6H_2O$), ethanol, chloroform ($CHCl_3$), ferrous chloride tetrahydrate ($FeCl_2.4H_2O$), ammonia (28%), hexadecyltrimethylammonium bromide (CTAB), and oleic acid (OA) were purchased from the Chinese Academy of Medical Sciences (Shanghai). Triethanolamine (TEA), ethyl acetate, tetraethyl orthosilicate (TEOs), and methanol were purchased from DAMAO Chemical Reagent Factory (Tianjin). Lead nitrate, lead citrate, sodium hydroxide, hydrochloric acid, and nitric acid were purchased from the Beijing Institute of Chemical Reagents (Beijing). 3-Aminopropyltriethoxysilane (APTES) was obtained from Aladdin (Shanghai). DMEM, RIPA lysis buffer, trypsin, and FBS were obtained from Gibco (NY, United States). The MTT test kit was purchased from Solarbio (Beijing). The Bradford protein assay kit, ROS, MDA, SOD, and GSH-Px test kits were obtained from Jiancheng (Nanjing). Glutaraldehyde and uranyl acetate were purchased from Micxy reagent (Chengdu). The human embryonic kidney cell line (HEK293) was purchased from the Cell Resource Center of Shanghai (Shanghai).

Synthesis of Amino-Functionalized Mesoporous Magnetic Nanoparticles

The OA-grafted Fe_3O_4 NPs (OA-Fe_3O_4) were synthesized, according to the reference with a minor modification (Wang et al., 2020). Typically, 4.60 g of $FeCl_3.6H_2O$ and 1.80 g of $FeCl_2.4H_2O$ were added to 35 ml of deionized water. Then, 0.80 ml of OA and 20 ml of $NH_3.H_2O$ (14 wt%) were added to the solution. The solution was heated up to 95°C for 2 h under a nitrogen atmosphere. The black product was collected with a magnet and then dispersed in $CHCl_3$ (70 mg mL^{-1}).

Then, 0.6 ml of the prepared $CHCl_3$ solution was added to 5.5 ml of water containing CTAB (20.0 mg mL^{-1}). The solution was then heated up to 62°C to completely evaporate the residual $CHCl_3$. Then, 25 ml of water and 65 μg of TEA were added to the mixture and was heated up to 85°C for 20 min. Next, 1 ml of TEOs and 3 ml of ethyl acetate were subsequently added and reacted for 2 h before the as-prepared Fe_3O_4@SiO_2 NPs were collected by a magnet followed by washing. Then, 80 μL of hydrochloric acid were added to the solution (20 ml) at 80°C and stirred for 9 h to remove CTAB in the mesoporous silica coating. The final products were washed by ethanol to remove the residual reactants and preserved in ethanol for use (150 mg mL^{-1}).

In addition, 0.5 ml of APTES was added to 20 ml of the aforementioned ethanol solution containing Fe_3O_4@$mSiO_2$ NPs. The mixture of the solution kept reacting for 4 h at 70°C. The final production of Fe_3O_4@$mSiO_2$-NH_2 NPs was washed with water before drying up in an oven at 65°C.

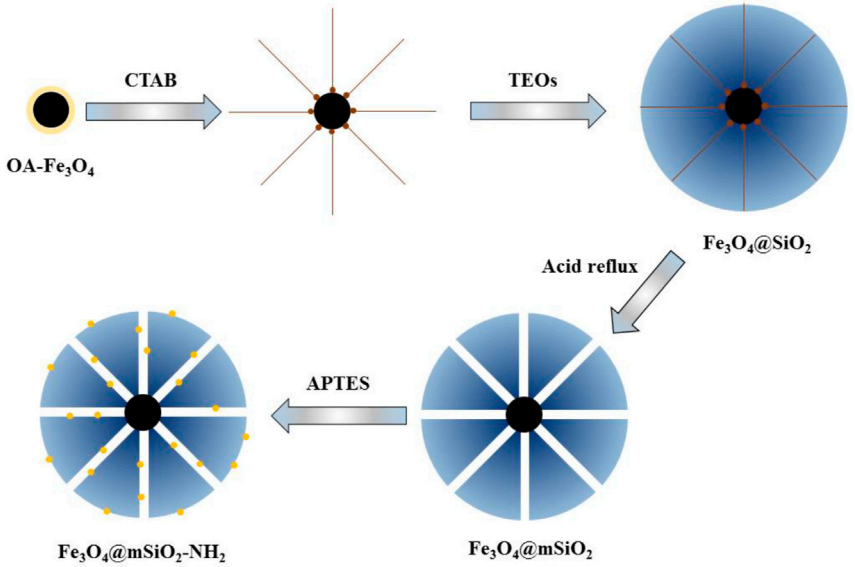

SCHEME 1 | Diagram of the synthesis procedure of Fe_3O_4@mSiO_2-NH_2 NPs.

Adsorption of Pb^{2+} Ions

For the adsorption assay, we prepared an acidified stock solution of lead nitrate (500 mg L^{-1} of Pb^{2+} ions). The Pb^{2+} ion concentration was adjusted from 20 to 400 mg L^{-1} with pH = 6 adjusted by nitric acid (wt 5%) and sodium hydroxide (wt 5%). Then, 20 mg of Fe_3O_4@mSiO_2-NH_2 NPs was added to each 20 ml of Pb^{2+} ion solution, which was then shaken at 200 rpm at 25°C for 6 h. The Fe_3O_4@mSiO_2-NH_2 NPs were removed using a magnet and dried at 25°C.

Characterization

The surface morphologies of NPs and cells were recorded by scanning electron microscopy (SEM) (JSM-6510) and transmission electron microscopy (TEM) (JEOL JEM-2100F). The Fourier transform infrared spectrum (FT-IR) was investigated from 500 to 4,000 cm^{-1} on a Nicolet Impact 410 FTIR spectrometer. The concentrations of Pb^{2+} ions were investigated with inductively coupled plasma-optical emission spectroscopy (ICP-OES) (iCAP 7000 Series). Powder X-ray diffraction (XRD) analysis was determined by using a Rigaku D-Max 2550 diffractometer. Nitrogen adsorption-desorption isotherms were obtained in ASAP 2020. The magnetic properties of as-prepared samples were recorded by using a SQUID-VSM magnetometer. A microplate reader (Bio-Rad 550) was used for the MTT assay.

Cell Culture Conditions

HEK293 cells were cultivated with DMEM with 10% FBS and then cultivated at 37°C (of 5% CO_2). The medium was refreshed per day, and the HEK293 cells were subcultured at the ratio of 1:2 every 2 or 3 days for use.

Cellular Uptake

Location and qualitative analyses of intracellular nanoparticles were demonstrated by TEM. HEK293 cells were collected and incubated for 12 h. Then, the initial DMEM of the cells was replaced by the sample DMEM, and the sample cells were cultivated for 12 h. HEK293 cells were fixed with glutaraldehyde before being laid up for 4.5 h in darkness and then made into ultrathin sample sections after being dehydrated. The sample sections dyed with uranyl acetate and lead citrate were obtained.

Cell Viability

A certain amount of diluted solution of lead nitrate (100 μg mL^{-1}) was added to DMEM at the ratio of 1:10, and DMEM samples with Pb^{2+} ion concentrations of 5.0 and 7.5 μg mL^{-1} were obtained. Fe_3O_4@mSiO_2-NH_2 NPs and Pb^{2+} ion-adsorbed Fe_3O_4@mSiO_2-NH_2 NPs were dispersed in deionized water (1000 μg mL^{-1}). Then, a certain quantity of NP solution was added to DMEM to obtain the DMEM samples mixed with Fe_3O_4@mSiO_2-NH_2 NPs (50 and 75 μg mL^{-1}, respectively). Finally, six DMEM samples were obtained.

Moreover, 96-well cell culture plates were applied to cultivate cells which were cultivated at 37°C for over 10 h in a humid chamber containing 5% CO_2, until they adhered onto the plates. Then, the culture medium was replaced by each of the prepared mediums, followed by cultivating the cells for 24 h. Blank medium wells were set as the negative control group. To measure the cell viability, 10 μL of the MTT reagent was added to each well of cell culture plates, and HEK293 cells were cultivated for 1.5 h. The absorbance of cell samples at 450 nm was obtained by using a microplate reader.

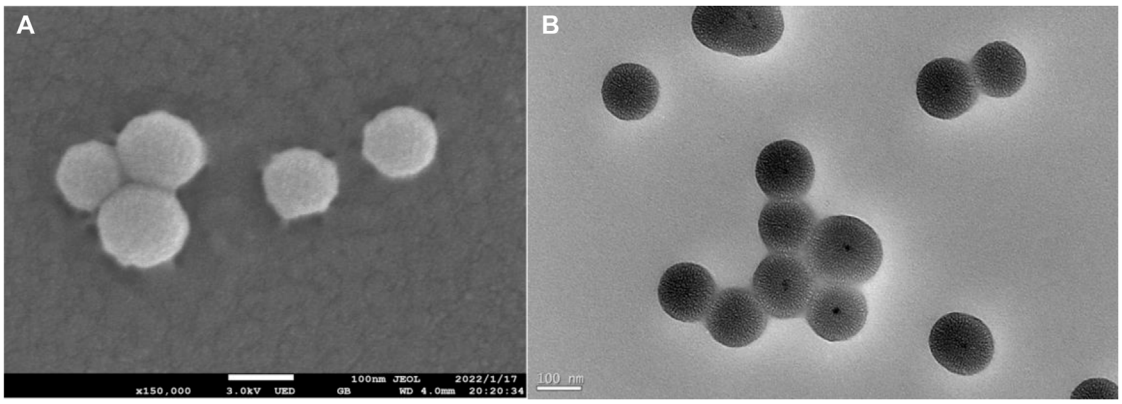

FIGURE 1 | (A) SEM image of Fe_3O_4@mSiO_2-NH_2 NPs and **(B)** TEM image of Fe_3O_4@mSiO_2-NH_2 NPs.

Biochemical Parameters for Oxidative Stress

The intracellular oxidative stress (OS) was assessed by the ROS level, MDA level, activity of SOD, and GSH-Px activity. In brief, HEK293 cells were exposed to the DMEM samples and washed with ice-cold PBS, followed by being lysed. The supernatants were obtained after centrifugation for the measurements of oxidative stress. Finally, MDA, SOD, GSH-Px, and SOD were tested, according to the instructions of the kits.

In brief, the fluorescence intensity of dichlorofluorescein (DCF) can reflect the ROS level of cells. Affected by intracellular lipase, intracellular dichlorodihydrofluorescein diacetate (DCFH-DA) will hydrolyze into dichlorofluorescein diacetate (DCFH), which will be further oxidized into DCF by active oxygen in cells. Under certain conditions, MDA will react with thiobarbituric acid (TBARS). The red light adsorbing products will be measured to reflect the content of MDA. GSH-Px activity assay can be evaluated by the content of a yellow compound with maximum absorption at 405 nm, which forms after GSH-Px reacts with dithionitrobenzoic acid (DTNB). The SOD activity assay is based on a formazan dye color reaction. SOD inhibits the formation of the formazan dye by reacting with O^{2-}, which will oxidize the WST-1 reagent into formazan dye originally.

Statistical Analysis

SPSS 21.0 was used for all the statistical analyses. Data were expressed as mean ± SD from three independent experiments. The *t*-test was applied for analyzing the statistical differences. The statistical significance was set as $p < 0.05$.

RESULTS

Microstructure Observation

Fe_3O_4 NPs were synthesized by a one-pot co-precipitation method, followed by enclosing mesoporous silica shell and grafting amino groups**.** The Fe_3O_4@mSiO_2-NH_2 NPs were spherical with a silica shell, as shown in **Figure 1A**. The TEM image (**Figure 1B**) depicts that well-dispersed OA-Fe_3O_4 NP cores with diameters of less than 10 nm are enclosed by a silica shell, forming Fe_3O_4@mSiO_2-NH_2 NPs with a diameter of 125 ± 25 nm. In addition, there exists a mesoporous structure in Fe_3O_4@mSiO_2-NH_2 NPs.

Structure and Magnetic Properties

The chemical compositions of samples were investigated by FT-IR (**Figure 2A**). The absorption peak at 560 cm^{-1} in the spectrum was due to the Fe-O stretch, indicating the existence of Fe_3O_4 particles in both NPs. The peaks at 806 and 1098 cm^{-1} corresponded to the stretch and vibration of Si–O–Si and Si–O groups in the silica coatings (Wang et al., 2020). The characteristic peak at 1626 cm^{-1} in both spectra was due to the vibration of Si-OH groups or adsorbed water (Yuan et al., 2014; Li et al., 2021). The peaks that appeared at 1487 and 1553 cm^{-1} for the Fe_3O_4@mSiO_2-NH_2 were ascribed to the stretch and vibration of NH_2 (Yuan et al., 2014), proving the successful graft of amino groups on the silica shell. The peak at 3373 cm^{-1} was attributed to the vibrations of amine N-H (Yu et al., 2012). The stretching mode that appeared at 3450 cm^{-1} was attributed to the H_2O molecule (Wu et al., 2014; Yuan et al., 2014; Wang S et al., 2021). Adsorption peaks at 2858 and 2931 cm^{-1} corresponded to the -CH_2- group (Wang S et al., 2021).

Figure 2B shows the XRD result of as-prepared samples. Corresponding to the spinel structure of the magnetite phase, the diffraction peaks of OA-Fe_3O_4 NPs at 30.4°, 35.7°, 43.3°, 53.7°, 57.5°, and 62.9° were related to their indices of (220), (311), (400), (422), (511), and (440), respectively (Enache et al., 2017). There was a wide diffraction band observed at 22–26° ascribing to the amorphous silica coating, which led to the weakness of Fe_3O_4 diffraction peaks (Yuan et al., 2014; Enache et al., 2017).

The results of magnetic properties for the OA-Fe_3O_4 NPs and Fe_3O_4@mSiO_2-NH_2 NPs are shown in **Figure 2C**. The magnetic hysteresis loops indicated that both the NPs were superparamagnetic (Wang et al., 2020). The magnetic saturation (M_s) value of Fe_3O_4@mSiO_2-NH_2 was 6.28 emu·g^{-1}, which was much lower than that of OA-Fe_3O_4 (52.63 emu·g^{-1}).

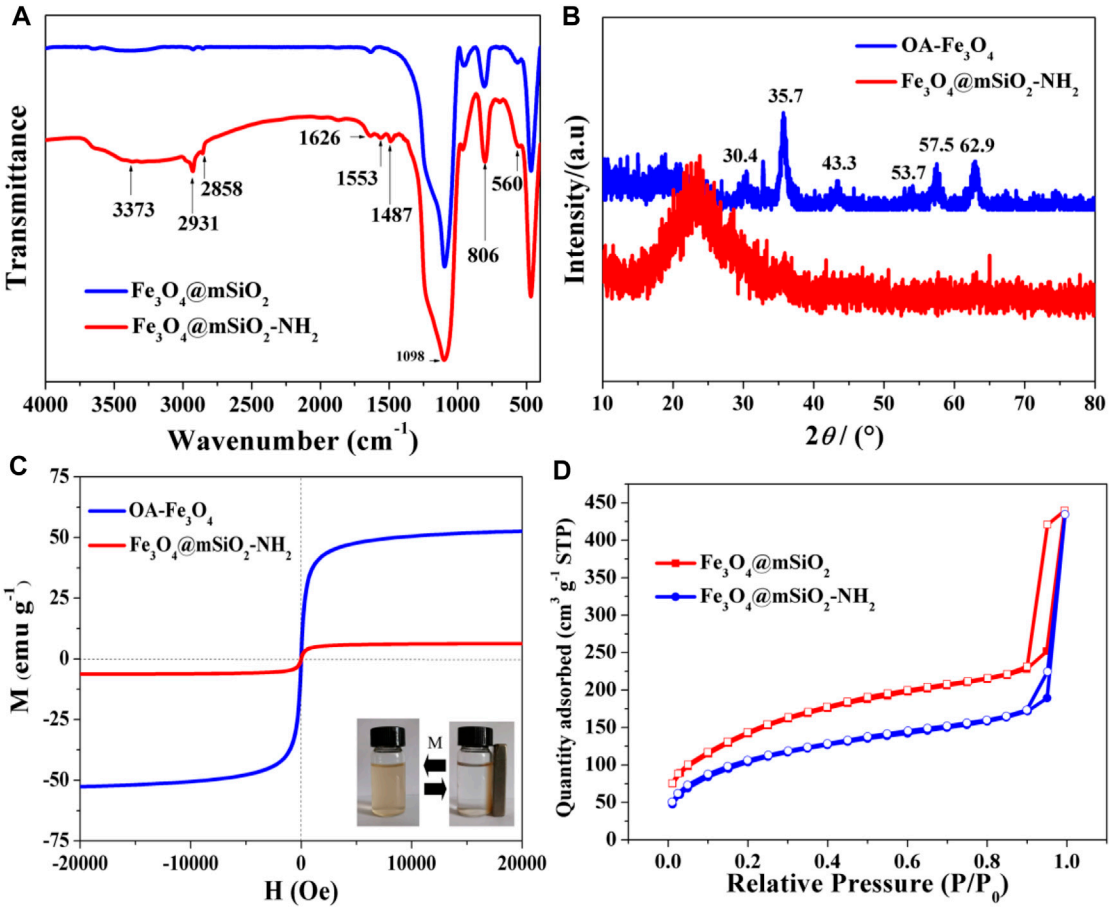

FIGURE 2 | (A) FT-IR spectra of Fe_3O_4@mSiO$_2$ NPs and Fe_3O_4@mSiO$_2$-NH$_2$ NPs. **(B)** XRD patterns and **(C)** magnetic hysteresis loops of OA-Fe_3O_4 NPs and Fe_3O_4@mSiO$_2$-NH$_2$ NPs. The digital images are Fe_3O_4@mSiO$_2$-NH$_2$ NPs that are dispersed in water and gathered by using a magnet. **(D)** N_2 adsorption isotherms of Fe_3O_4@mSiO$_2$ NPs and Fe_3O_4@mSiO$_2$-NH$_2$ NPs.

TABLE 1 | Texture properties of Fe3O4@mSiO2 NPs and Fe3O4@mSiO2-NH2 NPs.

Sample	SBET (m^2·gF02D^{-1})	Pore size (nm)	Vp (cm^3·gF02D^{-1})
Fe3O4@mSiO2 NPs	511.95	3.4	0.68
Fe3O4@mSiO2-NH2 NPs	377.47	3.0	0.67

This result can be ascribed to the silica shell outside the OA-Fe_3O_4 NPs (**Figure 1B**).

The texture characteristics of Fe_3O_4@mSiO$_2$ NPs and amino-grafted NPs were measured by N_2 adsorption-desorption. The N_2 adsorption isotherms of the two kinds of NPs suggested that both of them possessed a mesoporous structure (**Figure 2D**). The Brunauer–Emmett–Teller (BET) surface area of Fe_3O_4@mSiO$_2$ NPs was 511.95 m^2/g, which was larger than that of Fe_3O_4@mSiO$_2$-NH$_2$ NPs (377.47 m^2/g). The average pore diameter of the initial NPs was 3.4 nm, which was larger than that of amino-grafted NPs (3.0 nm, **Table 1**). These results depicted that the amino groups were modified on the silica shell successfully, which agreed well with the result of FT-IR (**Figure 2A**).

Adsorption Ability

To evaluate the proper proportion of Pb^{2+} ions adsorbed on Fe_3O_4@mSiO$_2$-NH$_2$, the adsorption assays were conducted under the condition of 25°C with a pH value of 6. Langmuir and Freundlich models were used to fit the data of the adsorption. The Langmuir model is expressed as **Equation 1**:

$$\frac{C_e}{Q_e} = \frac{C_e}{Q_m} + \frac{1}{Q_m K_L}, \quad (1)$$

where Q_e (mg·g^{-1}) is the adsorption capacity of Fe_3O_4@mSiO$_2$-NH$_2$ NPs at equilibrium; C_e (mg·L^{-1}) is the equilibrium concentration of Pb^{2+} ions; Q_m (mg·g^{-1}) is the monolayer adsorption capacity of Fe_3O_4@mSiO$_2$-NH$_2$ NPs; and K_L (L·mg^{-1}) is the Langmuir parameter.

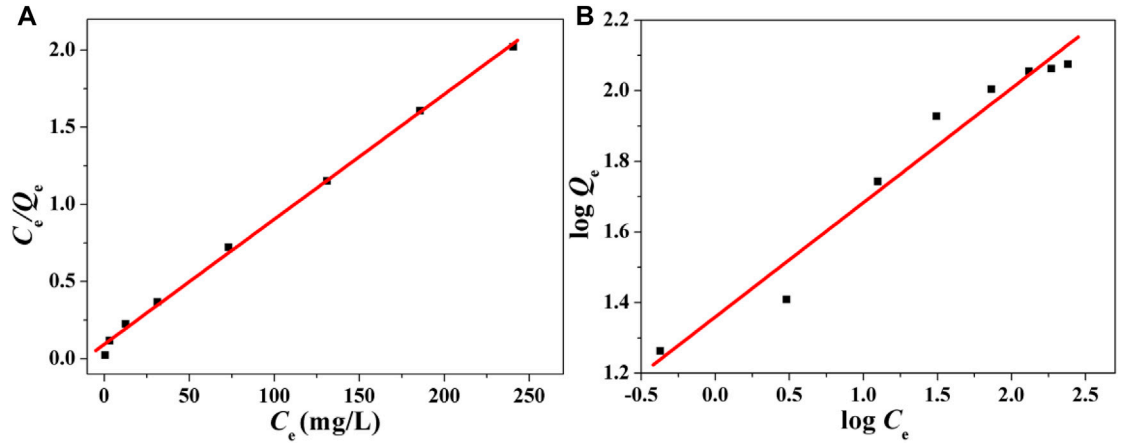

FIGURE 3 | (A) Langmuir isotherm for Pb^{2+} ion adsorption on Fe_3O_4@$mSiO_2$-NH_2 NPs and **(B)** Freundlich isotherm.

TABLE 2 | Langmuir and Freundlich parameters.

Langmuir isotherm			Freundlich isotherm		
Qm (mg·gF02D^{-1})	**KL (L·mgF02D^{-1})**	**R^2**	**KF (mg·gF02D^{-1})·(L·mg)1/n**	**N**	**R^2**
123.460	0.086	0.997	22.890	0.324	0.958

Freundlich model is expressed as **Equation 2**:

$$\log Q_e = \log K_F + n \log C_e, \quad (2)$$

where Q_e (mg·g^{-1}) and C_e (mg·L^{-1}) are the same as that in the Langmuir isotherm model; K_F (mg·g^{-1}) (L·mg^{-1})$^{1/n}$ and n are the Freundlich parameters.

To calculate the adsorption constants of Fe_3O_4@$mSiO_2$-NH_2 NPs, linearized Langmuir and Freundlich plots were fitted, as shown in **Figure 3**. As can be seen from **Table 2**, the Langmuir model-fitted equilibrium adsorption data are better. This result proves that the adsorption of Pb^{2+} on Fe_3O_4@$mSiO_2$-NH_2 NPs belongs to the monolayer adsorption process, which is caused by electrostatic adsorption. Furthermore, the interaction between neighboring Pb^{2+} ions is weak. The maximum adsorption capacity (Q_m) reaches 123.46 mg g^{-1}.

In this work, the Fe_3O_4@$mSiO_2$-NH_2 NPs with Pb^{2+} ion weight of 10% were taken as an example to investigate the effect of the adsorbed Pb^{2+} ions on the cytotoxicity of Fe_3O_4@$mSiO_2$-NH_2 NPs to HEK293 cells.

Cell Viability and Morphology

The results of cell viability are shown in **Figure 4A**. The viabilities of the HEK293 cells cultivated with Pb^{2+} ion concentrations of 5 (**Figure 4A**, named as Pb5) and 7.5 μg mL^{-1} (**Figure 4A**, named as Pb7.5) decreased to 89.9% and 80.1% compared to the control group (**Figure 4A**, named as control), respectively. The viabilities of HEK293 cells cultured with Fe_3O_4@$mSiO_2$-NH_2 NPs of 50 (**Figure 4A**, named as NPs50) and 75 μg mL^{-1} (**Figure 4A**, named as NPs75) increased to 119.9 % and 108.1%, respectively. On the contrary, the viabilities of cells cultured with Pb^{2+} ion-adsorbed Fe_3O_4@$mSiO_2$-NH_2 NPs of 50 (**Figure 4A**, named as NPs50-Pb5) and 75 μg mL^{-1} (**Figure 4A**, named as NPs75-Pb7.5) decreased to 97.1 % and 84.7%, respectively. It is noticeable that at a higher Pb^{2+} ion dosage (e.g., Pb7.5 and NPs75-7.5), there are no significant differences in cell viability ($p > 0.05$, **Figure 4A**). But the significant difference occurs when the dosage of Pb^{2+} ions is lower (e.g., Pb5 and NPs50-5; $p < 0.05$; **Figure 4A**).

To observe the changes in cell morphology, images of cell samples were taken by using an optic microscope (**Figure 4B**). Compared to the control (**Figure 4B**), no obvious change in the morphology of the HEK293 cells cultivated with Pb7.5 was observed. But the cell density slightly decreased, which was consistent with the results of the MTT assay (**Figure 4A**). In contrast, there was almost no effect on the morphology and the density of the HEK293 cells when cultivated with NPs75 and NPs75-Pb7.5 (**Figure 4B**), respectively, depicting that the adsorption weakened the effects of Pb^{2+} ions to HEK293 cells.

Cellular Uptake

The location and internalization of NPs are shown in **Figure 5**. Clusters composed of accumulated NPs with a diameter of 300–700 nm were observed in the cytoplasm (**Figures 5C,D**), suggesting that the NPs could be internalized by HEK293 cells without damaging the morphology of the cells.

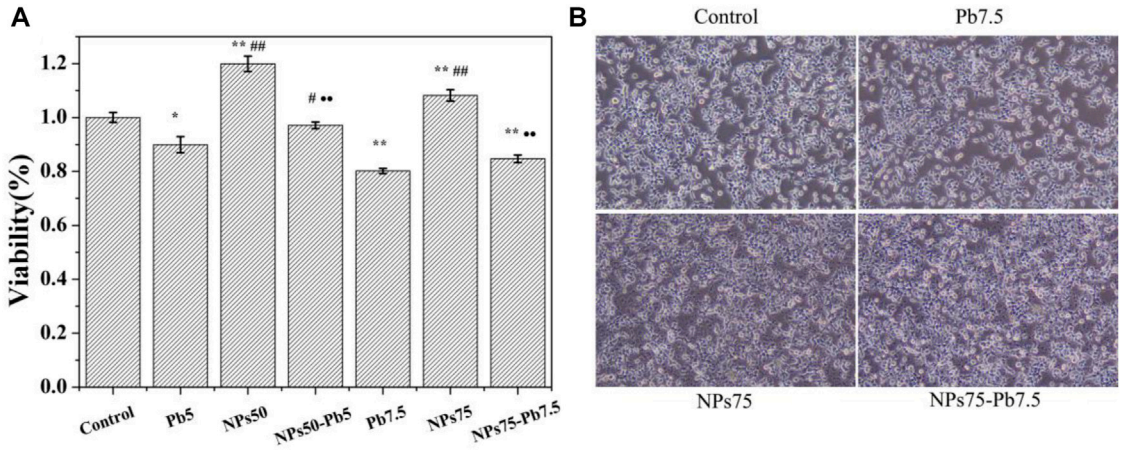

FIGURE 4 | (A) Viability of HEK293 cells. Control is the control samples. Pb5 is cells cultivated with Pb^{2+} ions in the concentration of 5 μg mL^{-1}. NPs50 is cells cultivated with Fe_3O_4@$mSiO_2$-NH_2 NPs in the concentration of 50 μg mL^{-1}. NPs50-Pb5 is cells cultivated with Pb^{2+} ion-adsorbed Fe_3O_4@$mSiO_2$-NH_2 NPs in the concentration of 50 μg mL^{-1}. Pb7.5, NPs75, and NPs75-Pb7.5 are cell samples cultivated with Pb^{2+} ions, Fe_3O_4@$mSiO_2$-NH_2 NPs, and Pb^{2+} ion-adsorbed Fe_3O_4@$mSiO_2$-NH_2 NPs in the concentrations of 7.5, 75 and 75 μg mL^{-1}, respectively. *vs.* control (*$p < 0.05$ and **$p < 0.01$). $^{\#}$*vs.* Pb5 or Pb7.5, corresponding to the concentration of NPs of 50 or 75 μg mL^{-1}, respectively ($^{\#}p < 0.05$ and $^{\#\#}p < 0.01$). ¨*vs.* NPs50 or NPs75 corresponding to the concentration of NPs of 50 or 75 μg mL^{-1}, respectively (¨$p < 0.05$ and ¨$p < 0.01$). **(B)** Morphology of cell samples control, Pb7.5, NPs75, and NPs75-Pb7.5.

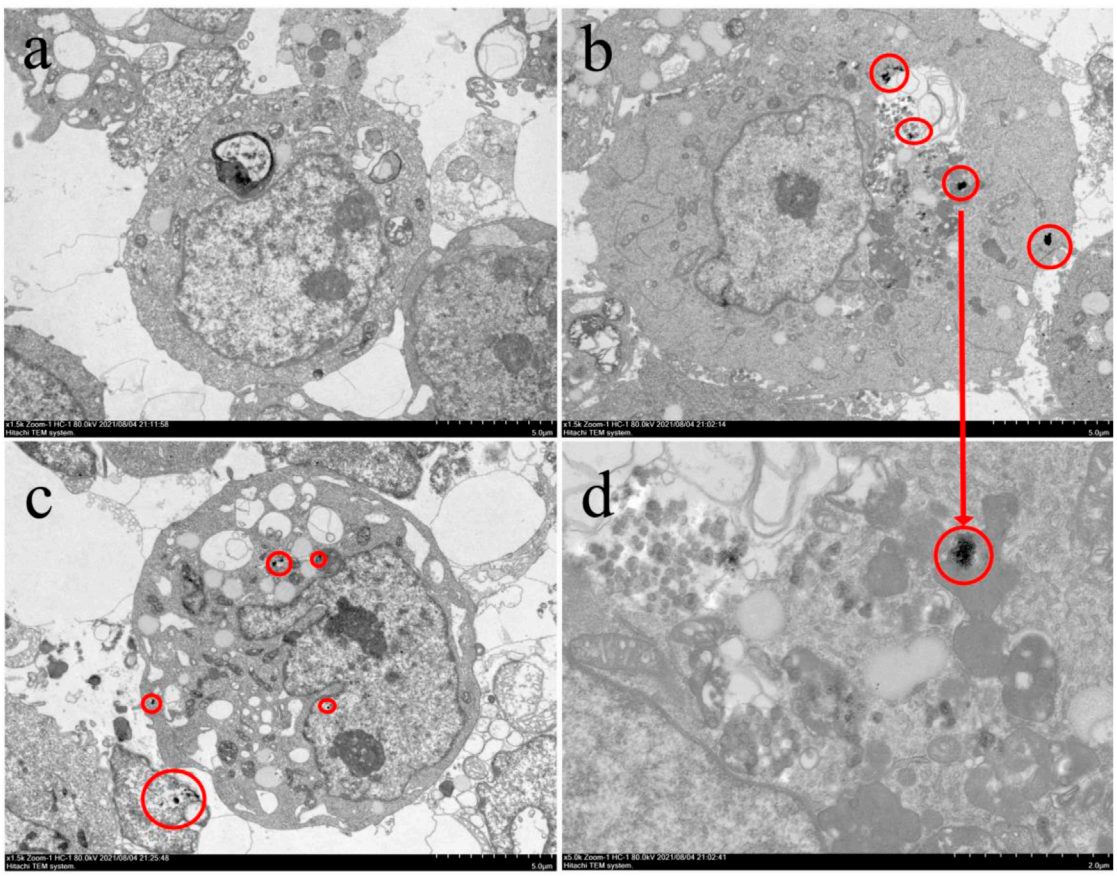

FIGURE 5 | TEM image of **(A)** cells of control, **(B)** cells of NPs75, **(C)** cells of NPs75-Pb7.5, and **(D)** enlargement of NPs75. The inner NPs clusters are circled in red.

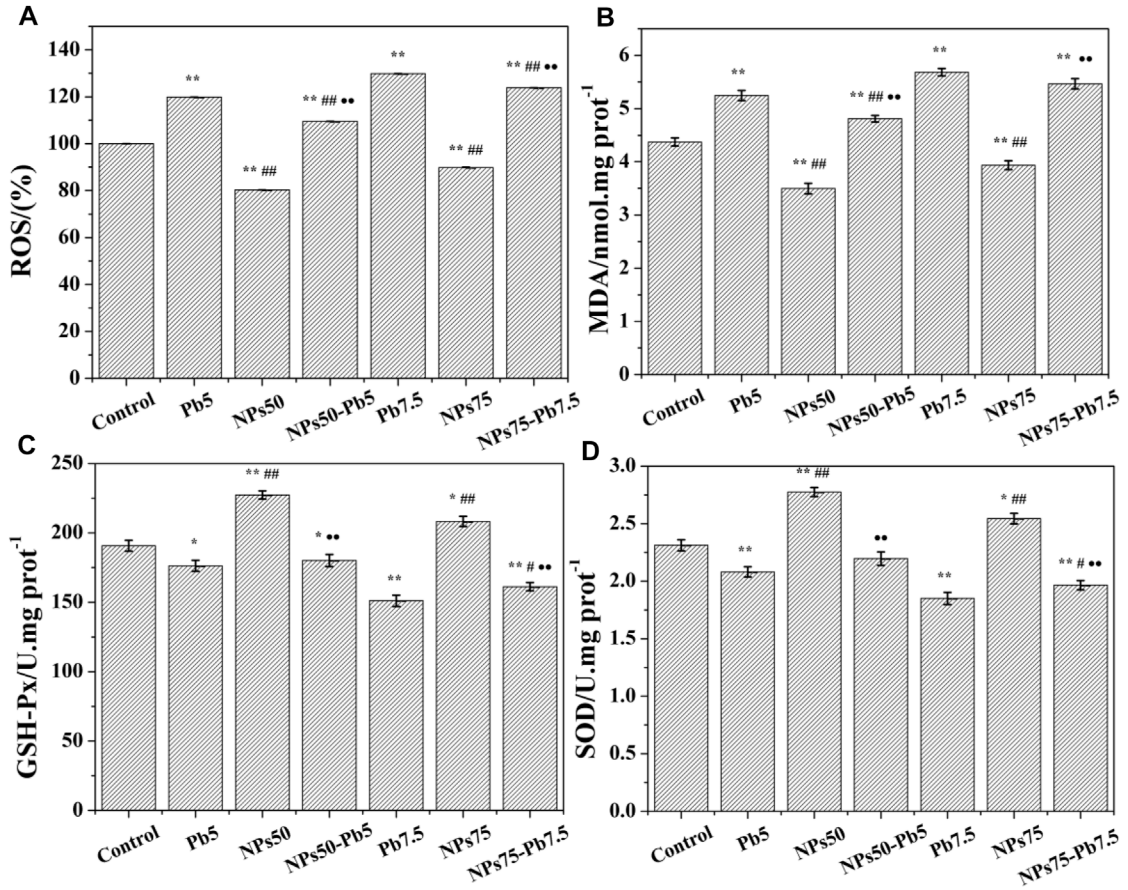

FIGURE 6 | (A) Quantitative level of intracellular ROS. **(B)** MDA level. **(C)** Intracellular GSH-Px activity. **(D)** SOD enzyme activity. **vs.* control (*$p < 0.05$ and **$p < 0.01$). $^{\#}$*vs.* Pb5 or Pb7.5, corresponding to the concentration of NPs of 50 or 75 μg mL^{-1}, respectively ($^{\#}p < 0.05$ and $^{\#\#}p < 0.01$). ¨*vs.* NPs50 or NPs75, corresponding to the concentration of NPs of 50 or 75 μg mL^{-1}, respectively ($p < 0.05$ and ¨$p < 0.01$).

Biochemical Parameters for Oxidative Stress

To further demonstrate the difference in cytotoxicity of Pb^{2+} ions, Fe_3O_4@mSiO_2-NH_2 NPs, and Pb^{2+} ion-adsorbed Fe_3O_4@mSiO_2-NH_2 NPs to HEK293 cells, the oxidative stress (OS) of HEK293 cells was investigated by measuring ROS, MDA, SOD, and GSH-Px of cells. As shown in **Figure 6**, most samples exhibit a significant difference compared to the control ($p < 0.05$), in a dose-dependent manner. When cultured with Pb5 and Pb7.5, the ROS (**Figure 6A**) and MDA (**Figure 6B**) of HEK293 cells increased, while GSH-Px (**Figure 6C**) and SOD (**Figure 6D**) activities of HEK293 cells decreased. Meanwhile, NPs50 and NPs75 inhibited the oxidative stress as ROS (**Figure 6A**) and significantly decreased MDA (**Figure 6B**), but the GSH-Px (**Figure 6C**) and SOD (**Figure 6D**) activities increased. When cultured by the Pb^{2+} ion-adsorbed Fe_3O_4@mSiO_2-NH_2 NPs, the OS level of HEK293 cells was lower than that incubated by the dissociative Pb^{2+} ions (**Figure 6**). For example, the ROS levels of HEK293 cells cultured with NPs50-Pb5 and NPs75-Pb7.5 were 109.5% and 123.8%, respectively, while those of Pb5 and Pb7.5 increased to 119.9% and 129.8%, respectively.

DISCUSSION

Previous work reported that the NPs could be internalized by cells through endocytic processes and gather in endocytic vesicles (Valsami-Jones and Lynch, 2015). Various factors affected the internalization process including particle size (Nel et al., 2006; Kim et al., 2014), shape (Nel et al., 2006), and surface modification (Nel et al., 2006; Foglia et al., 2017). For instance, the spherical nanoparticles were easier to be internalized than the ones in columnar shape (Chithrani et al., 2006). The particles with larger size (e.g., > 200 nm) were hard to enter cells, thus exhibiting less toxicity than that with smaller size (Dong et al., 2017). Pang et al. (2011) found that particles with sizes less than 40 nm could enter the nucleus. In this work, the NPs were successfully internalized into the cytoplasm without damaging the cell membrane because of the small size (125 ± 25 nm) and spherical morphology (**Figures 5C,D**), but they were too large to enter the nucleus.

The cytotoxicity of heavy metal ion–adsorbed magnetic mesoporous silica NPs might be caused by the internalized NPs due to their ultrafine sizes and various surface properties (Passagne et al., 2012; Shin et al., 2021). OS was considered to be

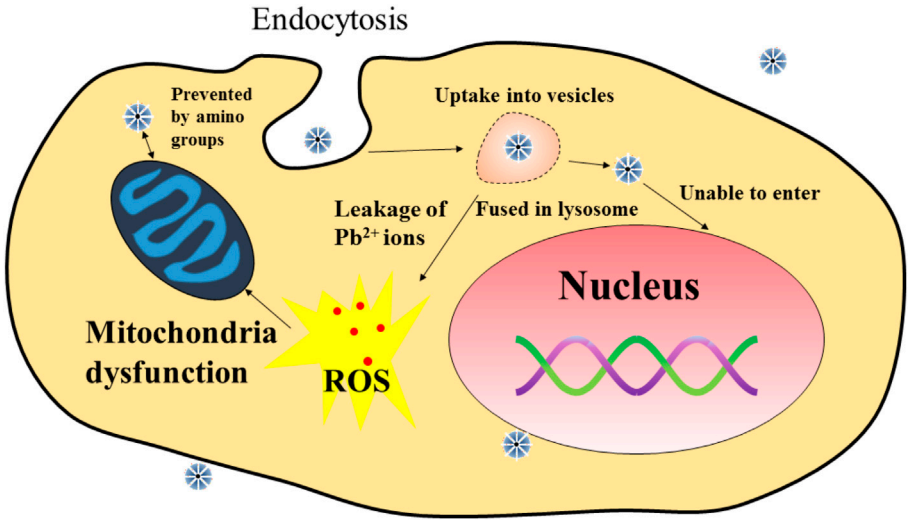

FIGURE 7 | Process of the Pb^{2+} ions adsorbed on NPs inducing ROS in cells.

one of the main mechanisms to evaluate the cytotoxicity caused by NPs and the co-contaminants, which could be measured by the ROS level, MDA level, GSH-Px activity, and SOD activity (Wu et al., 2016; Zhu et al., 2019; Ahamed et al., 2020).

Wang et al. (2020) proved that silica NPs could increase intracellular ROS levels and decrease the activity of the GSH content, which exhibited a dose-dependent cytotoxicity to mammalian cell lines. In our work, Fe_3O_4@$mSiO_2$-NH_2 NPs exhibited non-cytotoxicity to HEK293 cells, according to the MTT assays (**Figure 4A**, NPs50 and NPs75) and the tests of OS parameters (**Figure 6**), indicating amino groups made a positive impact on the process of cell proliferation (Manke et al., 2013; Gonzalez et al., 2019). It can be explained that amino groups may act as a protective shell to prevent the NPs from contacting organelles, thus inhibiting the reactions between NPs and organelles (Zhu et al., 2012).

NPs50-Pb5 exhibited non-toxicity in MTT assays compared to control, but NPs75-Pb7.5 decreased the cell viability to 84.7% of the control, which was attributed to the lower dosage of Pb^{2+} ions in NPs50-Pb5 (**Figures 4A, 6**) (Zhang H et al., 2014). However, OS measurements showed that the adsorbed Pb^{2+} ions could affect the generation of ROS and inhibit the activity of GSH-Px even at a lower concentration such as NPs50-Pb5 (**Figures 6A–C**), suggesting Pb^{2+} ion-adsorbed Fe_3O_4@$mSiO_2$-NH_2 NPs in fact showed a negative effect on HEK293 cells.

Metal ions leaked from NPs are also considered as one of the main reasons causing cytotoxicity since they would react with enzymes and induce OS in cells (Zhang H et al., 2014; Sharma et al., 2015; Premshekharan et al., 2017; Zhang et al., 2018; Gonzalez et al., 2019). Compared to the initial NPs, the viabilities of cells decreased dramatically (**Figure 4A**), and the OS level increased significantly ($p < 0.05$) along with the increase in the dosage of Pb^{2+} ion-adsorbed NPs (**Figure 6**), indicating that the adsorbed Pb^{2+} ions might leak from Fe_3O_4@$mSiO_2$-NH_2 NPs, which reacted with enzymes (e.g., GSH-Px and SOD enzyme) in HEK293 cells, triggering OS in HEK293 cells eventually. As shown in **Figure 7**, the possible mechanism of the leakage of metal ions from NPs can be explained that the engulfed NPs are stocked in endocytic vesicles and fused with the lysosome. The degradation of enzymes and the acidic atmosphere in the lysosome will lead to the leakage of metal ions (Wang et al., 2013), which induces the generation of OH and ROS metabolites. These products will inhibit the activity of antioxidant enzymes and finally lead to OS of HEK293 cells (Liu et al., 2012).

Although the desorption of Pb^{2+} ions might occur in HEK293 cells, the viabilities of NPs50-Pb5 and NPs75-Pb7.5 were higher than those of the cells cultured with the dissociative Pb^{2+} ions of 5.0 and 7.5 $\mu g\,mL^{-1}$, respectively (**Figure 4A**), indicating the adsorbed Pb^{2+} ions were not completely desorbed from the NPs in HEK293 cells. The ROS, MDA, GSH-Px, and SOD tests (**Figure 6**) were consistent with the MTT assays except for the groups of Pb7.5 and NPs75-Pb7.5, suggesting lipolysis was not inhibited when cells were incubated with a higher concentration of Pb^{2+} ions (**Figure 6B**). All the results demonstrated that the adsorption by Fe_3O_4@$mSiO_2$-NH_2 NPs could prevent Pb^{2+} ions from inducing OS in HEK293 cells and subsequently inhibit the cytotoxicity of Pb^{2+} ions to HEK293 cells.

CONCLUSION

Our study proved that Fe_3O_4@$mSiO_2$-NH_2 NPs with a size of 125 ± 25 nm could be internalized by HEK293 cells and gathered together in the cytoplasm. There was no cytotoxicity to HEK293 cells found when cells were cultivated with Fe_3O_4@$mSiO_2$-NH_2 NPs. On the contrary, they inhibited the oxidative stress of HEK293 cells. But the viability of HEK293 cells decreased significantly when the dosage of Fe_3O_4@$mSiO_2$-NH_2 NPs was

increased. Pb^{2+} ion-adsorbed Fe_3O_4@$mSiO_2$-NH_2 NPs exhibited significant dose-dependent cytotoxicity to HEK293 cells, which was attributed to the intracellular OS process. For instance, ROS of NPs50-Pb5 and NPs75-Pb7.5 reached 109.5% and 123.9% of the control, respectively. Meanwhile, MDA increased with the decrease in GSH-Px and SOD activities, suggesting that desorption of Pb^{2+} ions might occur in cells. But the adsorbed Pb^{2+} ions on NPs exhibited lower cytotoxicity to HEK293 cells than dissociative Pb^{2+} ions. The Fe_3O_4@$mSiO_2$-NH_2 nanoparticles showed no cytotoxicity to HEK293 cells, and the adsorption of Fe_3O_4@$mSiO_2$-NH_2 NPs reduced the cytotoxicity of Pb^{2+} ions depending on the dosage. Our work provides a better understanding of the cytotoxicity of Pb^{2+}-adsorbed nanoparticles and assesses the risk to human beings when using engineered nanoparticles for wastewater treatments.

DATA AVAILABILITY STATEMENT

The original contributions presented in the study are included in the article/Supplementary Material; further inquiries can be directed to the corresponding author.

AUTHOR CONTRIBUTIONS

All authors listed have made a substantial, direct, and intellectual contribution to the work and approved it for publication.

FUNDING

This work was supported by the Energy Bureau of Jilin Province of China (No.3D516L911425).

REFERENCES

Ahamed, M., Akhtar, M. J., and Alhadlaq, H. A. (2020). Influence of Silica Nanoparticles on Cadmium-induced Cytotoxicity, Oxidative Stress, and Apoptosis in Human Liver HepG2 Cells. *Environ. Toxicol.* 35, 599–608. doi:10.1002/tox.22895

Ahamed, M., Akhtar, M. J., and Alhadlaq, H. A. (2019). Preventive Effect of TiO_2 Nanoparticles on Heavy Metal Pb-Induced Toxicity in Human Lung Epithelial (A549) Cells. *Toxicol. Vitro* 57, 18–27. doi:10.1016/j.tiv.2019.02.004

Almasian, A., Najafi, F., Mirjalili, M., Gashti, M. P., and Fard, G. C. (2016). Zwitter Ionic Modification of Cobalt-Ferrite Nanofiber for the Removal of Anionic and Cationic Dyes. *J. Taiwan Inst. Chem. Eng.* 67, 306–317. doi:10.1016/j.jtice.2016.07.037

Brännvall, M. L., Bindler, R., Renberg, I., Emteryd, O., Bartnicki, J., and Billström, K. (1999). The Medieval Metal Industry Was the Cradle of Modern Large-Scale Atmospheric Lead Pollution in Northern Europe. *Environ. Sci. Technol.* 33, 4391–4395. doi:10.1021/es990279n

Bundschuh, M., Filser, J., Lüderwald, S., McKee, M. S., Metreveli, G., Schaumann, G. E., et al. (2018). Nanoparticles in the Environment: where Do We Come from, where Do We go to? *Environ. Sci. Eur.* 30, 1–17. doi:10.1186/s12302-018-0132-6

Cheng, T., Gao, H., Liu, G., Pu, Z., Wang, S., Yi, Z., et al. (2022). Preparation of Core-Shell Heterojunction Photocatalysts by Coating CdS Nanoparticles onto $Bi_4Ti_3O_{12}$ Hierarchical Microspheres and Their Photocatalytic Removal of Organic Pollutants and Cr (VI) Ions. *Colloid. Surf. A* 633, 127918. doi:10.1016/j.colsurfa.2021.127918

Cheng, T., Ma, Q., Gao, H., Meng, S., Lu, Z., Wang, S., et al. (2022). Enhanced Photocatalytic Activity, Mechanism and Potential Application of Idoped-$Bi_4Ti_3O_{12}$ Photocatalysts. *Mat. Today Chem.* 23, 100750. doi:10.1016/j.mtchem.2021.100750

Chithrani, B. D., Ghazani, A. A., and Chan, W. C. (2006). Determining the Size and Shape Dependence of Gold Nanoparticle Uptake into Mammalian Cells. *Nano Lett.* 6 (4), 662–668. doi:10.1021/nl052396o

Di, L., Sun, X., Xian, T., Li, H., Gao, Y., and Yang, H. (2021). Preparation of Z-Scheme Au-Ag_2S/Bi_2O_3 Composite by Selective Deposition Method and its Improved Photocatalytic Degradation and Reduction Activity. *Adv. Powder Technol.* 32 (10), 3672–3688. doi:10.1016/j.apt.2021.08.018

Dong, C. D., Tsai, M. L., Chen, C. W., and Hung, C. M. (2017). Heterogeneous Persulfate Oxidation of BTEX and MTBE Using Fe_3O_4− CB Magnetite Composites and the Cytotoxicity of Degradation Products. *Int. Biodet. Biodegr.* 124, 109–118. doi:10.1016/j.ibiod.2017.05.004

Enache, D. F., Vasile, E., Simonescu, C. M., Răzvan, A., Nicolescu, A., Nechifor, A. C., et al. (2017). Cysteine-functionalized Silica-Coated Magnetite Nanoparticles as Potential Nanoadsorbents. *J. Solid State Chem.* 253, 318–328. doi:10.1016/j.jssc.2017.06.013

Facchi, D. P., Cazetta, A. L., Canesin, E. A., Almeida, V. C., Bonafé, E. G., Kipper, M. J., et al. (2018). New Magnetic chitosan/alginate/Fe_3O_4@ SiO_2 Hydrogel Composites Applied for Removal of Pb (II) Ions from Aqueous Systems. *Chem. Eng. J.* 337, 595–608. doi:10.1016/j.cej.2017.12.142

Feng, L., Yang, X., Shi, Y., Liang, S., Zhao, T., Duan, J., et al. (2018). Co-exposure Subacute Toxicity of Silica Nanoparticles and Lead Acetate on Cardiovascular System. *Int. J. Nanomed.* 13, 7819. doi:10.2147/IJN.S185259

Foglia, S., Ledda, M., Fioretti, D., Iucci, G., Papi, M., Capellini, G., et al. (2017). *In Vitro* biocompatibility Study of Sub-5 Nm Silica-Coated Magnetic Iron Oxide Fluorescent Nanoparticles for Potential Biomedical Application. *Sci. Rep.* 7, 1–13. doi:10.1038/srep46513

Gao, H. J., Wang, S. F., Fang, L. M., Sun, G. A., Chen, X. P., Tang, S. N., et al. (2021). Nanostructured Spinel-type M (M= Mg, Co, Zn) Cr_2O_4 Oxides: Novel Adsorbents for Aqueous Congo Red Removal. *Mater. Today Chem.* 22, 100593. doi:10.1016/j.mtchem.2021.100593

Gonzalez, C. G., Álvarez, G. S., Camporotondi, D. E., Foglia, M. L., Aimé, C., Diaz, L. E., et al. (2019). Preliminary Evaluation of Median Lethal Concentrations of Stöber Silica Particles with Various Sizes and Surface Functionalities Towards Fibroblast Cells. *Silicon* 11, 2307–2312. doi:10.1007/s12633-014-9203-5

He, Y., and Park, K. (2016). Effects of the Microparticle Shape on Cellular Uptake. *Mol. Pharm.* 13, 2164–2171. doi:10.1021/acs.molpharmaceut.5b00992

Inglezakis, V. J., Loizidou, M. D., and Grigoropoulou, H. P. (2003). Ion Exchange of Pb^{2+}, Cu^{2+}, Fe^{3+}, and Cr^{3+} on Natural Clinoptilolite: Selectivity Determination and Influence of Acidity on Metal Uptake. *J. Colloid Interf. Sci.* 261, 49–54. doi:10.1016/S0021-9797(02)00244-8

Kim, J. E., Kim, H., An, S. S. A., Maeng, E. H., Kim, M. K., and Song, Y. J. (2014). *In Vitro* cytotoxicity of SiO_2 or ZnO Nanoparticles with Different Sizes and Surface Charges on U373MG Human Glioblastoma Cells. *Int. J. Nanomed.* 9, 235. doi:10.2147/IJN.S57936

Krętowski, R., Kusaczuk, M., Naumowicz, M., and Cechowska-Pasko, M. (2021). The Pro-Apoptotic Effect of Silica Nanoparticles Depends on Their Size and Dose, as Well as the Type of Glioblastoma Cells. *Int. J. Mol. Sci.* 22, 3564. doi:10.3390/ijms22073564

Li, J., Wang, S., Sun, G., Gao, H., Yu, X., Tang, S., et al. (2021). Facile Preparation of $MgAl_2O_4$/CeO_2/Mn_3O_4 Heterojunction Photocatalyst and Enhanced Photocatalytic Activity. *Mat. Today Chem.* 19, 100390. doi:10.1016/j.mtchem.2020.100390

Li, L., Gao, H., Liu, G., Wang, S., Yi, Z., Wu, X., et al. (2022). Synthesis of Carnation Flower-like $Bi_2O_2CO_3$ Photocatalyst and its Promising Application for Photoreduction of Cr (VI). *Adv. Powder Technol.* 33 (3), 103481. doi:10.1016/j.apt.2022.103481

Li, L., Sun, X., Xian, T., Gao, H., Wang, S., Yi, Z., et al. (2022). Template-free Synthesis of $Bi_2O_2CO_3$ Hierarchical Nanotubes Well-Orderedly Self-Assembled from Nanoplates for Promising Photocatalytic Application. *Phys. Chem. Chem. Phys.* 24, 8279. doi:10.1039/D1CP05952A

Li, Y. H., Di, Z., Ding, J., Wu, D., Luan, Z., and Zhu, Y. (2005). Adsorption Thermodynamic, Kinetic and Desorption Studies of Pb^{2+} on Carbon Nanotubes. *Water Res.* 39, 605–609. doi:10.1016/j.watres.2004.11.004

Liu, C. M., Ma, J. Q., and Sun, Y. Z. (2012). Puerarin Protects Rat Kidney from Lead-Induced Apoptosis by Modulating the PI3K/Akt/eNOS Pathway. *Toxicol. Appl. Pharm.* 258, 330–342. doi:10.1016/j.taap.2011.11.015

Liu, H., Wang, Q., and Zhang, F. (2020). Preparation of Fe_3O_4@ SiO_2@ P (AANa-Co-AM) Composites and Their Adsorption for Pb (II). *ACS Omega* 5 (15), 8816–8824. doi:10.1021/acsomega.0c00403

Liu, H., Wang, S., Gao, H., Yang, H., Wang, F., Chen, X., et al. (2022). A Simple Polyacrylamide Gel Route for the Synthesis of $MgAl_2O_4$ Nanoparticles with Different Metal Sources as an Efficient Adsorbent: Neural Network Algorithm Simulation, Equilibrium, Kinetics and Thermodynamic Studies. *Sep. Purif. Technol.* 281, 119855. doi:10.1016/j.seppur.2021.119855

Lu, C. F., Yuan, X. Y., Li, L. Z., Zhou, W., Zhao, J., Wang, Y. M., et al. (2015). Combined Exposure to Nano-Silica and Lead Induced Potentiation of Oxidative Stress and DNA Damage in Human Lung Epithelial Cells. *Ecotox. Environ. Safe.* 122, 537–544. doi:10.1016/j.ecoenv.2015.09.030

Ma, L., Zhou, M., He, C., Li, S., Fan, X., Nie, C., et al. (2019). Graphene-based Advanced Nanoplatforms and Biocomposites from Environmentally Friendly and Biomimetic Approaches. *Green Chem.* 21, 4887–4918. doi:10.1039/C9GC02266J

Manke, A., Wang, L., and Rojanasakul, Y. (2013). Mechanisms of Nanoparticle-Induced Oxidative Stress and Toxicity. *Biomed. Res. Int.* 2013, 942916. doi:10.1155/2013/942916

Maria das Graças, A. K., de Andrade, J. B., de Jesus, D. S., Lemos, V. A., Bandeira, M. L., dos Santos, W. N., et al. (2006). Separation and Preconcentration Procedures for the Determination of Lead Using Spectrometric Techniques: A Review. *Talanta* 69, 16–24. doi:10.1016/j.talanta.2005.10.043

Nel, A., Xia, T., Madler, L., and Li, N. (2006). Toxic Potential of Materials at the Nanolevel. *Science* 311, 622–627. doi:10.1126/science.1114397

Pandey, S., Fosso-Kankeu, E., Spiro, M. J., Waanders, F., Kumar, N., Ray, S. S., et al. (2020). Equilibrium, Kinetic, and Thermodynamic Studies of Lead Ion Adsorption from Mine Wastewater onto MoS_2-Clinoptilolite Composite. *Mat. Today Chem.* 18, 100376. doi:10.1016/j.mtchem.2020.100376

Pang, Z., Gao, H., Yu, Y., Chen, J., Guo, L., Ren, J., et al. (2011). Brain Delivery and Cellular Internalization Mechanisms for Transferrin Conjugated Biodegradable Polymersomes. *Int. J. Pharm.* 415, 284–292. doi:10.1016/j.ijpharm.2011.05.063

Passagne, I., Morille, M., Rousset, M., Pujalté, I., and Lazou, B. (2012). Implication of Oxidative Stress in Size-dependent Toxicity of Silica Nanoparticles in Kidney Cells. *Toxicology* 299, 112–124. doi:10.1016/j.tox.2012.05.010

Patrick, L. (2006). Lead Toxicity, a Review of the Literature. Part I: Exposure, Evaluation, and Treatment. *Alter. Med. Rev.* 11, 2–22. doi:10.1016/j.jep.2005.09.015

Premshekharan, G., Nguyen, K., Zhang, H., Forman, H. J., and Leppert, V. J. (2017). Low Dose Inflammatory Potential of Silica Particles in Human-Derived THP-1 Macrophage Cell Culture Studies–Mechanism and Effects of Particle Size and Iron. *Chemico-biolog. Inter.* 272, 160–171. doi:10.1016/j.cbi.2017.05.004

Sharma, M., Poddar, M., Gupta, Y., Nigam, S., Avasthi, D. K., Adelung, R., et al. (2020). Solar Light Assisted Degradation of Dyes and Adsorption of Heavy Metal Ions from Water by CuO–ZnO Tetrapodal Hybrid Nanocomposite. *Mat. Today Chem.* 17, 100336. doi:10.1016/j.mtchem.2020.100336

Sharma, V. K., Filip, J., Zboril, R., and Varma, R. S. (2015). Natural Inorganic Nanoparticles–Formation, Fate, and Toxicity in the Environment. *Chem. Soc. Rev.* 44, 8410–8423. doi:10.1039/C5CS00236B

Shin, T. H., Ketebo, A. A., Lee, D. Y., Lee, S., Kang, S. H., Basith, S., et al. (2021). Decrease in Membrane Fluidity and Traction Force Induced by Silica-Coated Magnetic Nanoparticles. *J. Nanobiotechnol.* 19, 1–14. doi:10.1186/s12951-020-00765-5

Slowing, I. I., Vivero-Escoto, J. L., Wu, C. W., and Lin, V. S. Y. (2008). Mesoporous Silica Nanoparticles as Controlled Release Drug Delivery and Gene Transfection Carriers. *Adv. Drug Ddeliv. Rev.* 60, 1278–1288. doi:10.1016/j.addr.2008.03.012

Sun, X., Di, L., Xian, T., Zhou, Y., Li, H., Gao, Y., et al. (2021). Enhanced Photocatalytic and Photo-Fenton Catalytic Activity of $BiFeO_3$ Polyhedron Decorated by AuAg Alloy Nanoparticles. *J. Mat. Sci. Mat. Electron.* 32 (1), 623–639. doi:10.1007/s10854-020-04844-z

Tang, F., He, T., Zhang, H., Wu, X., Li, Y., Long, F., et al. (2020). The MnO@N-Doped Carbon Composite Derived from Electrospinning as Cathode Material for Aqueous Zinc Ion Battery. *J. Electroanal. Chem.* 873, 114368. doi:10.1016/j.jelechem.2020.114368

Valsami-Jones, E., and Lynch, I. (2015). How Safe Are Nanomaterials? *Science* 350, 388–389. doi:10.1126/science.aad0768

Wang, B., Wei, Y., Wang, Q., Di, J., Miao, S., and Yu, J. (2020). Superhydrophobic Magnetic Core–Shell Mesoporous Organosilica Nanoparticles with Dendritic Architecture for Oil–Water Separation. *Mat. Chem. Front.* 4, 2184–2191. doi:10.1039/D0QM00246A

Wang, J., Wang, G., Wei, X., Liu, G., and Li, J. (2018). ZnO Nanoparticles Implanted in TiO_2 Macrochannels as an Effective Direct Z-Scheme Heterojunction Photocatalyst for Degradation of RhB. *Appl. Surf. Sci.* 456, 666–675. doi:10.1016/j.apsusc.2018.06.182

Wang, S. F., Chen, X. Y., Gao, H. J., Fang, L. M., Hu, Q. W., Sun, G. A., et al. (2021). A Comparative Study on the Phase Structure, Optical and NIR Reflectivity of $BaFe_{12}O_{19}$ Nano-Pigments by the Traditional and Modified Polyacrylamide Gel Method. *J. Nano Res.* 67, 1–14. doi:10.4028/www.scientific.net/jnanor.67.1

Wang, S., Gao, H., Li, J., Wang, Y., Chen, C., Yu, X., et al. (2021). Comparative Study of the Photoluminescence Performance and Photocatalytic Activity of $CeO_2/MgAl_2O_4$ Composite Materials with an Nn Heterojunction Prepared by One-step Synthesis and Two-step Synthesis Methods. *J. Phys. Chem. Solids* 150, 109891. doi:10.1016/j.jpcs.2020.109891

Wang, Z., Von Dem Bussche, A., Kabadi, P. K., Kane, A. B., and Hurt, R. H. (2013). Biological and Environmental Transformations of Copper-Based Nanomaterials. *ACS Nano* 7, 8715–8727. doi:10.1021/nn403080y

Wu, J., Shi, Y., Asweto, C. O., Feng, L., Yang, X., Zhang, Y., et al. (2016). Co-exposure to Amorphous Silica Nanoparticles and Benzo [a] Pyrene at Low Level in Human Bronchial Epithelial BEAS-2B Cells. *Environ. Sci. Pollut. Res.* 23, 23134–23144. doi:10.1007/s11356-016-7559-3

Wu, Q., Li, W., and Liu, S. (2014). Carboxyl-rich Carbon Microspheres Prepared from Pentosan with High Adsorption Capacity for Heavy Metal Ions. *Mat. Res. Bull.* 60, 516–523. doi:10.1016/j.materresbull.2014.09.015

Xian, T., Li, H., Gao, Y., Sun, X., Di, L., and Yang, H. (2022). Constructing a Novel AuAg/BiOBr/$BaTiO_3$ Composite via Selective Decoration Route with Enhanced Visible-Light Photoatalytic Performance. *Opt. Mat.* 123, 111842. doi:10.1016/j.optmat.2021.111842

Yu, J., Le, Y., and Cheng, B. (2012). Fabrication and CO_2 Adsorption Performance of Bimodal Porous Silica Hollow Spheres with Amine-Modified Surfaces. *RSC Adv.* 2, 6784–6791. doi:10.1039/C2RA21017G

Yuan, Q., Chi, Y., Yu, N., Zhao, Y., Yan, W., Li, X., et al. (2014). Amino-functionalized Magnetic Mesoporous Microspheres with Good Adsorption Properties. *Mat. Res. Bull.* 49, 279–284. doi:10.1016/j.materresbull.2013.08.063

Zhang, C., Shan, C., Jin, Y., and Tong, M. (2014). Enhanced Removal of Trace Arsenate by Magnetic Nanoparticles Modified with Arginine and Lysine. *Chem. Eng. J.* 254, 340–348. doi:10.1016/j.cej.2014.05.133

Zhang, H., Li, W., Xue, Y., and Zou, F. (2014). TRPC1 Is Involved in Ca^{2+} Influx and Cytotoxicity Following Pb^{2+} Exposure in Human Embryonic Kidney Cells. *Toxicol. Lett.* 229, 52–58. doi:10.1016/j.toxlet.2014.05.017

Zhang, J., Wang, S., Gao, M., Li, R., and Liu, S. (2018). Multihierarchically Profiling the Biological Effects of Various Metal-Based Nanoparticles in Macrophages under Low Exposure Doses. *ACS Sustain. Chem. Eng.* 6, 10374–10384. doi:10.1021/acssuschemeng.8b01744

Zhu, J., Zhao, Y., Gao, Y., Li, C., Zhou, L., Qi, W., et al. (2019). Effects of Different Components of PM2. 5 on the Expression Levels of NF-κB Family Gene mRNA and Inflammatory Molecules in Human Macrophage. *Int. J. Environm. Res. Public Heal.* 16, 1408. doi:10.3390/ijerph16081408

Zhu, X. M., Wang, Y. X. J., Leung, K. C. F., Lee, S. F., Zhao, F., Wang, D. W., et al. (2012). Enhanced Cellular Uptake of Aminosilane-Coated Superparamagnetic Iron Oxide Nanoparticles in Mammalian Cell Lines. *Int. J. Nanomed.* 7, 953. doi:10.2147/IJN.S28316

Conflict of Interest: The authors declare that the research was conducted in the absence of any commercial or financial relationships that could be construed as a potential conflict of interest.

Publisher's Note: All claims expressed in this article are solely those of the authors and do not necessarily represent those of their affiliated organizations, or those of the publisher, the editors, and the reviewers. Any product that may be evaluated in this article, or claim that may be made by its manufacturer, is not guaranteed or endorsed by the publisher.